ADVANCED ENERGY MATERIALS
www.advenergymat.de

Increasing the Pressure-Free Stripping Capacity of the Lithium Metal Anode in Solid-State-Batteries by Carbon Nanotubes

Till Fuchs, Catherine G. Haslam, Alexandra C. Moy, Christian Lerch, Thorben Krauskopf, Jeff Sakamoto, Felix H. Richter,* and Jürgen Janek**

Lithium metal is the key anode material for solid-state-batteries as its successful implementation will drastically increase their energy and power densities. However, anode contact loss during stripping leads to dendrites upon plating and subsequent cell failure. Design strategies to mitigate these issues are crucial to enable the use of lithium metal anodes. This paper reports the dissolution kinetics of composite anodes made of lithium metal and carbon nanotubes (CNTs) with a garnet-type solid electrolyte (SE). In addition to an enhancement of the effective diffusion within the anode, its dissolution is fundamentally changed from being 2D to 3D. By maintaining contact with the SE, the CNTs facilitate lithium transport to the interface, which yields more than 20 mAh cm^{-2} discharge capacity at 100 µA cm^{-2} without the application of external stack pressure (>1 MPa). Conclusions drawn from electrochemical data on the anode microstructure are validated using cryo-focused-ion-beam scanning electron microscopy and correlated with the mechanical properties. Microindentation, acoustic analysis, and stress–strain testing show that mechanical properties of the anode, like yield strength and hardness, are adjustable. Overall, it is shown that the mechanical and electrochemical properties of Li–CNT composite electrodes can be tailored to suit the requirements of a practical cell.

1. Introduction

Recently, all-solid-state batteries gained increasing attention as candidates to supersede lithium-ion-batteries as energy storage devices, for example, in the power train of electric vehicles.[1,2] While they are deemed to be safer and less flammable than lithium-ion batteries,[3] their main promise is that solid electrolytes (SEs) may enable the use of lithium metal as the anode material.[4,5] With 3861 mAh g^{-1}, lithium shows the highest theoretical capacity[6] as well as the lowest redox potential with −3.04 V versus the standard hydrogen electrode potential,[7] which makes it an attractive goal for the next generation of lithium batteries.

However, pore formation during lithium dissolution (stripping) and later dendrite growth triggered by the resulting heterogeneous interface hinders their application at high current densities so far.[8–10] For every lithium ion stripped from the electrode, a vacancy is "injected" in the metal. If the rate of vacancy injection, governed by the applied current density, is higher than the rate of vacancy annihilation by diffusion into the anode bulk,[8,11–13] vacancies accumulate at the interface — as originally shown by Janek and Majoni for the stripping of silver metal.[14] An accumulation of vacancies results in pore formation and contact loss, as well as facilitating dendrite formation upon current reversal.[4,10] To circumvent these issues, either the annihilation of vacancies from the interface needs to be accelerated or the local current density needs to be lowered. While the first mitigation strategy succeeds by applying stack pressures in the MPa range,[8,15,16] it is preferred to increase the vacancy annihilation rate by enhanced diffusion in the metal.

Increasing the lithium diffusion inside the electrode material to avoid pore formation is possible by alloying with other metals.[4,17] For example, 10 wt% of magnesium enhances the effective diffusion coefficient by a factor of three up to 2.3×10^{-11} cm^2 s^{-1}. However, due to different mechanical properties, pure lithium is superior to Li–Mg when external pressure in the MPa range is applied. As pressure most likely needs to be applied in large cell stacks, knowledge of the mechanical properties of the anode material is highly important. Careful modification of the lithium metal anode's elastic and plastic properties changes the sensitivity of cells

T. Fuchs, C. Lerch, T. Krauskopf, F. H. Richter, J. Janek
Institute of Physical Chemistry
Justus-Liebig-University Giessen
Heinrich-Buff-Ring 17, D-35392 Giessen, Germany
E-mail: Felix.H.Richter@pc.jlug.de; Juergen.Janek@pc.jlug.de
T. Fuchs, C. Lerch, T. Krauskopf, F. H. Richter, J. Janek
Center for Materials Research (ZfM)
Justus-Liebig-University Giessen
Heinrich-Buff-Ring 16, D-35392 Giessen, Germany
C. G. Haslam, A. C. Moy, J. Sakamoto
Department of Materials Science and Engineering
University of Michigan
Ann Arbor, MI 48109, USA
E-mail: jeffsaka@umich.edu
C. G. Haslam, J. Sakamoto
Department of Mechanical Engineering
University of Michigan
Ann Arbor, MI 48109, USA
The ORCID identification number(s) for the author(s) of this article can be found under https://doi.org/10.1002/aenm.202201125.

DOI: 10.1002/aenm.202201125

to applied stack pressures, opening up a variety of different applications with specific pressure requirements.

Instead of increasing the vacancy diffusion rate inside the anode or relying on the plastic flow or creep, it is also possible to lower the local current density by creating a 3D-architecture of the Li|SE-interface,[18] of which several approaches have been reported.[19–22] One example is the inner coating of a porous SE with carbon nanotubes (CNTs), which then act as a current collector for lithium nucleation.[19] Continuous plating and stripping of 5.0 mAh cm^{-2} with current densities up to 2.5 mA cm^{-2} based on the geometrical area was reported,[18] which is around five times that of planar interfaces.[4,23] However, the preparation of porous electrode configurations is challenging. Therefore, a planar electrode|SE interface is preferred, especially when considering stacked cell systems.

Additionally, CNTs can enhance the effective diffusion inside the metal electrode. Not only are lithium ions conducted within the walls of CNTs, but also lithium atom diffusion inside CNTs has been demonstrated.[6] When lithiated, CNTs are mixed ionic-electronic conductors (MIECs) and form a stable interface with lithium.[6,24] However, while well-engineered carbonaceous felts, membranes, or meshes wetted by lithium show a great improvement in anode performance,[25–27] the lithium transport mechanism and transport properties in these composites remain elusive.

In this work, we investigate the anodic dissolution and pore formation of composite anodes consisting of lithium metal and CNTs. It was possible to combine two approaches by 1) generating a CNT scaffold to obtain a MIEC 3D interface without the need for specially structured garnet SE and 2) accelerating lithium atom diffusion by mixing lithium metal with CNTs. With this heterogeneous solid-state composite, it was possible to strip more than 20 mAh cm^{-2} of lithium without the need for high applied external pressure and also tune the mechanical properties of the material, paving the way for the optimization of lithium electrodes.

2. Results and Discussion

2.1. Composite Characterization

The herein investigated composites were prepared by dispersing 10–40 wt% of multiwalled CNTs in liquid lithium metal at 350 °C and cooling of the resulting mixture to ambient temperature. During the mixing process, a distinct transition between nonwetting and wetting of the tubes in liquid lithium occurs. After the transition, the mixture appeared homogeneous and shiny to the naked eye (see Figure S1, Supporting Information). The measurement of the geometric density of the solidified mixtures shows a slight increase from around 0.54 g cm^{-3} for pure lithium to around 0.58 g cm^{-3} for Li–CNT30 (**Figure 1**a). During handling of the solidified composite, a decrease of ductility and increase in hardness compared with pure lithium metal was evident.

X-ray diffraction (XRD) measurements prove that both the CNTs and lithium metal keep their respective crystal structures, which indicates the chemical stability of the mixture. Both lithium and CNTs show specific and pronounced reflections which match with literature (Figure 1b).[17,28] From the reflections at 36.1°, 52.0°, and 64.9°, marked in grey, it is evident that the lithium crystal structure is still intact after preparing the composite electrode material and the lattice parameters have not changed either. This is reasonable, as no alloy is formed between the materials, which would most likely alter the lattice.[17]

The pure CNT powder shows broad reflections around 25.6°, 43.4°, and 53.4°, which correspond to the (002), (100), and (004) planes. As the indexing is based on the hexagonal graphite structure, (002) and (004) reflections correspond to an interplane and (100) to an intraplane distance.[29,30] Additionally, a slight asymmetry of the reflections to higher 2θ angles is observed for pure CNTs, which usually indicates nonideal stacking in turbostratic graphite layers.[29,31]

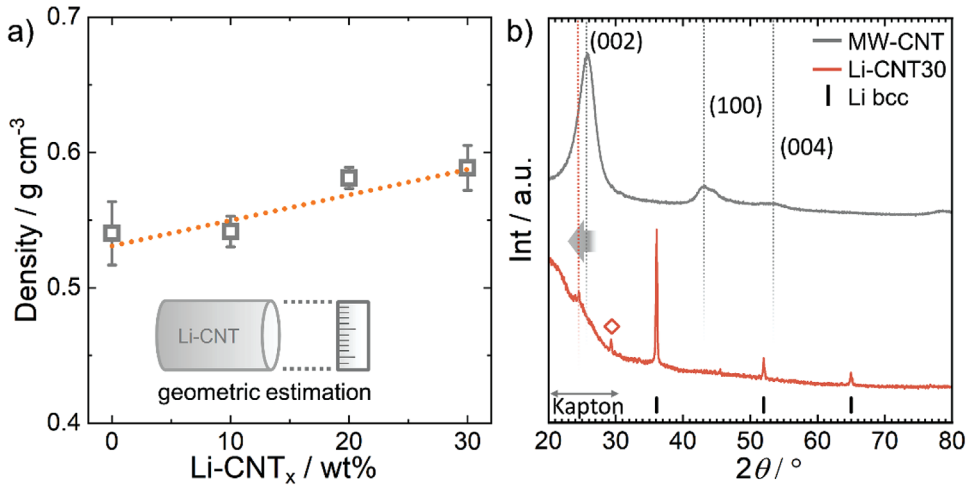

Figure 1. a) Density of the composite in dependence of the CNT content. The dashed line acts as a guide to the eye. b) The XRD pattern of the composite electrode Li–CNT30 is compared to that of pure CNTs and the reflection card of bcc lithium metal. The background increasing with small 2θ angles originates from the use of Kapton foil for air-tight sample preparation and is not indicative of the sample structure. A nonidentified impurity phase (presumably from reaction with atmosphere) also shows a reflection at 30°, marked with a diamond. The indexing of the CNT reflections is explained in Figure S1c,d, Supporting Information, regarding the (00l) and (d00) planes with an example CNT with three layers and a chirality of 20.

The reflection pattern of the composite shows that the CNT reflections both decrease in intensity and shift to higher 2θ angles. This indicates changes of the CNT structure. When calculating the CNT wall distance via the (002) reflection using the Bragg formula, an increase from 3.57 Å for the pristine state to 3.73 Å in the composite is observed. The increased distance corresponds well to the layer distance in lithiated graphite. We therefore assume that the CNTs are lithiated during the mixing process, and thus, also widened.[32,33] Likewise, lithiation of graphite coatings on SEs via liquid lithium was previously shown by Shao et al.[34] and is expected to occur at defects, holes, or at the end of the CNTs, which was shown for other graphitic structures.[35]

Additionally, the (002) reflection observed for the pristine CNT powder is broader than in the composite, as a shoulder at lower 2θ angles originates from the distance between different, separated CNTs.[36] When CNTs are incorporated into the lithium matrix this effect diminishes. In general, the XRD results show that the CNTs are lithiated in the composite and that the lithium matrix retains its crystal structure. To assess the electrochemical properties of the composites, impedance tests were carried out and shown in the next section.

2.2. Electrochemical Analysis of Impedance and Lithium Stripping

To analyze the dissolution and impedance of Li–CNT composite electrodes, Li_{id}|LLZO|Li–CNT cells were prepared, where the ideally reversible electrode (Li_{id}) shows negligible interfacial impedance, and thus, acts as a combined reference and counter electrode.[8,37] Therefore, any observed interfacial impedance and changes thereof solely originate from the Li–CNT|LLZO-interface. Using this method, the maximum current density is limited to around 200 µA cm^{-2}, as the Li_{id} anode is not resistant to dendrites at higher current densities. Foils of lithium for the preparation of the Li_{id} electrode and the Li–CNT composite were both prepared by mechanically flattening a chunk of each material, which was freed before from any passivation layer with a ceramic knife. In contrast to the high pressure utilized for Li_{id} (400 MPa) the herein prepared composite anode was initially pressed onto the pellet using a small hand pressing tool (≈30 MPa).

The impedance data of Li_{id}|LLZO|Li–CNT40 at 25 °C are shown in **Figure 2**a in the Nyquist representation alongside an equivalent circuit used for fitting. Lithium lanthanum zirconium oxide (LLZO) bulk and grain boundary (GB) contributions are identified at high (4 MHz) and middle (50 kHz) frequencies, respectively.[8,37] At low frequencies (1 kHz), a small interfacial contribution is observed. Hence, our equivalent circuit consists of a series combination of three parallel R–Q elements, where R and Q represent a resistor and nonideal capacity (constant-phase element). All obtained fit parameters are displayed in Table S1, Supporting Information. The apex frequencies and capacitances of the processes match well to data in the literature.[38] With only 27 Ω cm^2, the impedance for the Li–CNT40|LLZO interface is relatively low. This is remarkable as neither elevated temperature nor large pressures were utilized for the attachment of the Li–CNT40 electrode. Furthermore, the active contact area between lithium in the composite and LLZO might even be lower than geometrically estimated due to the lower area fraction of lithium at the interface.

Figure 2b shows an Arrhenius-plot of the three fitted impedance components. Note that the GB and interface processes are difficult to deconvolute as the interfacial resistance is small and the frequency ranges overlap. The linear fits of the graphs show that these are all temperature activated processes. The activation energies for bulk ($E_{A,Bulk}$ = 0.32 eV), GB ($E_{A,GB}$ = 0.41 eV) and interfacial transport ($E_{A,Int}$ = 0.37 eV) fit well to previously reported results.[8,37,39,40] It is reasonable that the Li–CNT|LLZO interface has a similar activation barrier as the Li|LLZO interface, as charge transfer occurs at the direct contact areas between lithium and LLZO.

The assessment of lithium dissolution is possible by long-term stripping experiments, which are performed on Li_{id}|LLZO|Li–CNT cells as a function of CNT weight fraction and current density. Electrodes were stripped until contact loss to the SE was observed, which is indicated by a steep increase in voltage and interfacial resistance (i.e., lithium depletion).[8,17,37] **Figure 3**a shows the voltage profiles when stripping with 100 µA cm^{-2} for Li and Li–CNT-composites. The displayed interfacial resistances are extracted via galvanostatic electrochemical impedance spectroscopy (GEIS) according to the fit procedure exemplified in Figure 2. The underlying evolution of the corresponding Nyquist and Bode plots is exemplarily shown for Li_{id}|LLZO|Li–CNT40 in Figures S2 and S3, Supporting Information. As seen therein, bulk and GB resistance contributions remain constant throughout the experiments,

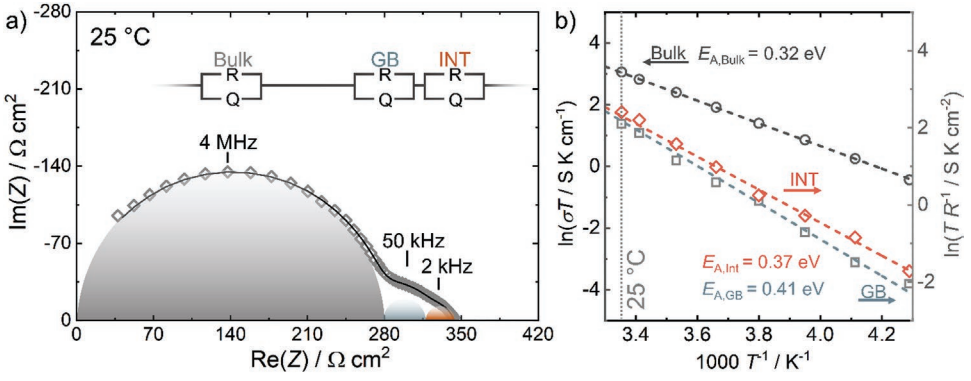

Figure 2. a) Nyquist plot of a Li_{id}|LLZO|Li–CNT40 cell together with the equivalent circuit for fitting. b) Arrhenius plot of impedance data for the bulk, grain boundary (GB), and interface (Int) processes as function of temperature.

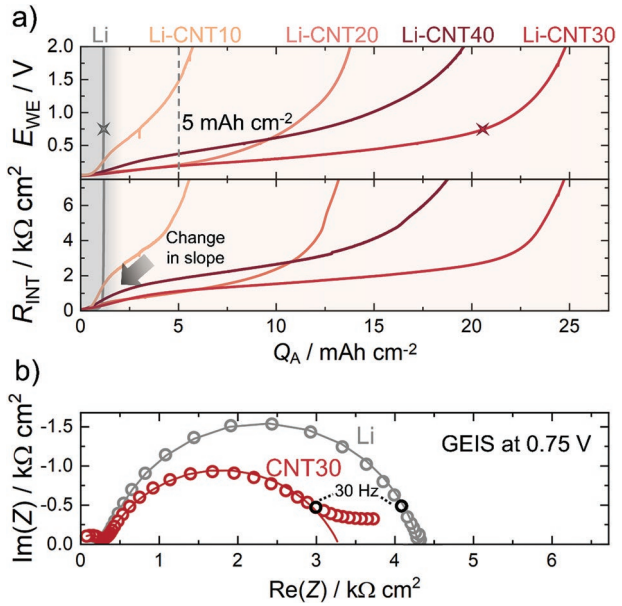

Figure 3. a) Voltage profiles during stripping of lithium, Li–CNT10, Li–CNT20, Li–CNT30, and Li–CNT40 at a current density of 100 µA cm^{-2} (top). The corresponding evolution of the interfacial resistance is shown underneath. b) Impedance spectra at 0.75 V (marked with stars in [a]) for lithium and Li–CNT30. Fitting was carried out similar to the impedance data shown in Figure 2.

which confirms that the Li_{id} counter electrode is stable and no dendrites are growing through the ceramic. Thus, for the fitting process, both bulk and GB resistance contributions were fixed to a constant value (determined from impedance measurements at the beginning).

While the lithium electrode reaches the 2 V cutoff (i.e., depletion) condition after only 1.2 mAh cm^{-2} (12 h of stripping), the composites delay the depletion by a factor of 20 to around 25 mAh cm^{-2} for Li–CNT30. This is the highest reported stripping capacity to date for an all-solid-state system. Albeit the current density is still quite low, the estimated target of 5 mAh cm^{-2} by Albertus et al. and Randau et al. is hereby exceeded.[2,41] Moreover, most of the stripping capacity in this experiment is available only after severe polarization and interfacial degradation already took place, which is not easily reversible. For pure lithium, the ratio of available capacity prior to degradation compared to the overall capacity is higher. Interestingly, the available capacity increases up to 30 wt% of CNTs being dispersed in lithium but decreases for Li–CNT40. Above a certain threshold, CNTs dispersed in lithium may not homogeneously be distributed anymore. Also, less lithium is present in the sample with higher CNT content.

Not only is a severe increase in stripping capacity observed for the Li–CNT composites, the overall voltage profile changes as well. While pure lithium shows a flat and stable plateau followed by a steep increase in voltage when contact is lost, changes of the electrode potential E_{WE} for the composites are more gradual. For the composites, there is an inflection point at around 1 mAh cm^{-2} where the slope changes. Interestingly, this corresponds well to the point where pure lithium loses the contact to the SE. Thereafter, the voltage and interface resistance gradually increase until the cutoff voltage is reached.

Both the time, t_{Kink}, of the inflection point and the time, t_{CL}, when full contact loss is reached can in principle be used to calculate the effective diffusion coefficient via Sand´s equation.[17,42,43] Therefore, Figure S4, Supporting Information, shows the stripping profiles of a Li–CNT30 electrode with 50–200 µA cm^{-2}. The characteristic inflection point occurs earlier during stripping with higher current density. Calculating the effective diffusion coefficient with t_{Kink} then yields $D_{eff,\,Kink} = (1.3 \pm 0.3) \times 10^{-11}$ cm^2 s^{-1}. This value can be understood as the effective Li diffusion coefficient of the composite electrode, which is nearly double that of pure lithium with $D_{eff,\,Li} = (0.8 \pm 0.1) \times 10^{-11}$ cm^2 s^{-11}. Therefore, the presence of the CNTs clearly improves Li diffusion in the anode. However, as the stripping mode changes at the inflection point, from direct stripping at the LLZO surface to stripping in the 3D Li–CNT network, the conditions are no longer fulfilled to properly interpret the time until full contact is lost in the manner of the Sands equation.

Changes in stripping are also visible in the impedance spectra acquired at 0.75 V during testing, depicted in Figure 3b. The impedance deviates from a semicircle below 30 Hz for Li–CNT30. This indicates changes of the constriction effect at the interface and therefore a difference in pore morphology. Further conclusions can be drawn from the Bode plot depicted in Figure S2, Supporting Information. After an initial emergence of the interface (constriction) resistance during stripping, its apex frequency remains roughly constant at around 2–3 kHz for Li–CNT40. In the case of pure lithium electrodes, this frequency shifts to higher frequencies at the end of the stripping process.[8] However, Li–CNT and Li–Mg both do not show the aforementioned frequency shift,[17] which is still elusive. The shift to higher frequencies observed for pure lithium electrodes may be explained by Joule heating of the few contact spots left, due to current focusing through these.[44,45] However, the contact spots after stripping Li–Mg alloys are more homogeneously distributed,[17] which should reduce the effect of Joule heating. Following this explanation, the contact spots after stripping Li–CNT electrodes should also be distributed more homogeneously as for Li–Mg when compared to lithium.

To evaluate the CNT influence on dendrite resilience, experiments on stripping and plating were carried out. Therefore, 0.2 mAh cm^{-2} were cycled in a Li–CNT30|LLZO:Ta|Li–CNT30 cell with increasing current densities (starting at 100 µA cm^{-2} and increasing by 100 µA cm^{-2} each step). As seen in Figure S5, Supporting Information, the cell experiences a short-circuit at around 600 µA cm^{-2}, which is in line with previous results on similar cell designs employing pure lithium as the anode material.[10,39] Thus, no clear effect on the dendrite resilience is observed using this test protocol.

Overall, the kink in the overpotential-capacity curve during stripping Li–CNT electrodes and their different low-frequency impedance are still elusive based on the electrochemical experiments alone. To analyze the stripping and resulting pore formation in more detail, top-view and cross-sectional images of the electrodes obtained by scanning electron microscopy (SEM) are discussed in the next section.

2.3. Differences of Pore Formation in Lithium and Lithium–CNT Composites

To understand the kink during stripping and resulting pore formation when using composite electrodes, their morphology was imaged using electron microscopy. **Figure 4** shows a schematic voltage profile for the stripping process with lithium and a composite. Shown alongside are top and cross-sectional focused-ion-beam SEM (FIB-SEM) images taken before and after depletion occurred during stripping. After depletion (contact loss, CL), the electrodes easily detach from the SE, which is not the case in the pristine state. Therefore, the surface visible in the top-view images is the face of the electrode, which previously was in contact with the LLZO.

The appearance of the as-prepared lithium and composite foils in the SEM images shown in Figure 4a,b is very similar. Both foils show a smooth surface with some bright lines, which most likely originate from the mechanical preparation. The cross-sectional images in Figure 4e,f show that both types of electrodes are free of pores. However, magnified images shown in Figure S6a,b, Supporting Information, display slight differences. It seems like curtaining and rippling, which occur during FIB-preparation,[46–48] lead to a more severe stair formation for the composite electrode. Rippling is frequently observed for carbon materials.[49–51] Furthermore, the top of the stairs shows a brighter contrast for the composite electrode, which hints at an accumulation of CNTs due to rippling and FIB-preparation.

After stripping had been performed until depletion, the surface morphologies of both electrodes deviate from each other. For pure lithium, large pores in the range of 5–15 µm are visible in the top-view image in Figure 4c, which correspond well to the typical morphology resulting in contact loss as observed in previous experiments.[8] On the contrary, the morphology of the stripped composite electrode displayed in Figure 4d rather shows smaller, deeper valleys in the material instead of pores at the surface. This larger pore volume is expected as around 20 mAh cm^{-2} or 0.8 mm^3 more lithium was stripped with this electrode. Figure S6d, Supporting Information, displays a higher magnification image of a similar Li–CNT30 electrode after stripping, showing that large parts of the surface only consist of a porous, fiber-like network. This is the residual CNT framework exposed after lithium was nearly completely stripped from the composite.

Cross-sectional images were additionally taken for lithium and Li–CNT40, respectively, as depicted in Figure 4g,h. No change in bulk morphology was observed for pure lithium when compared to the pristine sample in Figure 4e and Figure S6a, Supporting Information. This indicates that the stripping process for pure lithium only takes place at the direct interface to LLZO. However, cross-sectional images of the stripped Li–CNT40 depict a large gap and smaller closed pores in the 100–500 nm range fitting to the top-view micrographs. Another micrograph shows these pores at higher magnifications in Figure S6c, Supporting Information. Pores in this range were neither present in stripped lithium electrodes nor in pristine composites as displayed in Figure 4f. This confirms that closed porosity is generated only during the stripping process of Li–CNT electrodes. Overall, the depicted (FIB)-SEM images show clear differences in dissolution, as was indicated by electrochemical analysis. In the following, we propose a stripping mechanism for these composites based on the obtained results.

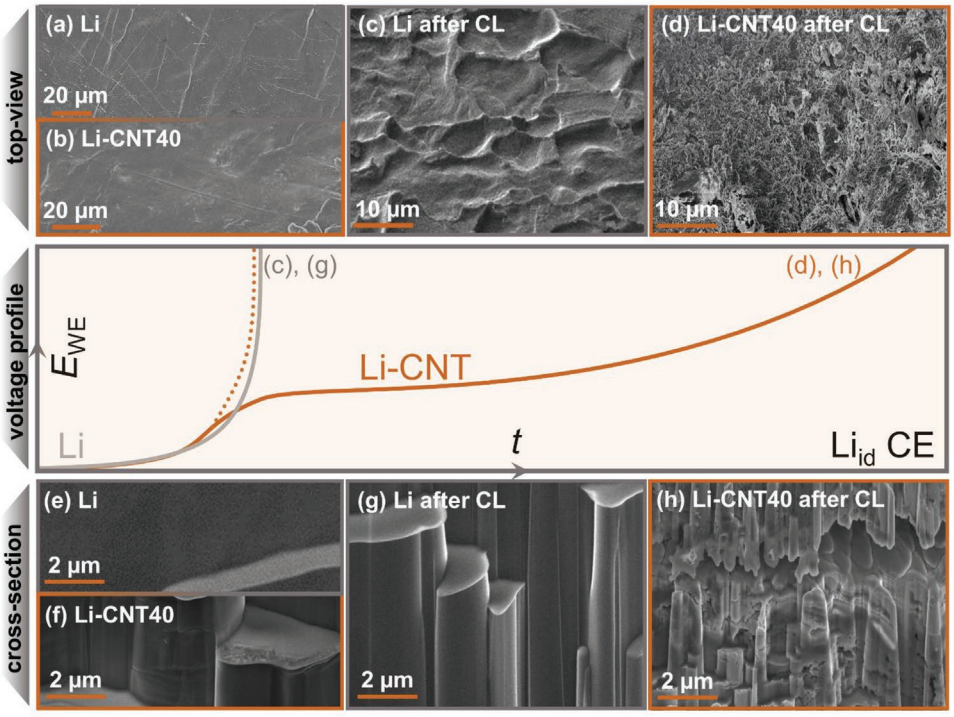

Figure 4. Top-view SEM images of the pristine state of a) lithium and b) Li–CNT40. Top-view SEM images of c) lithium and d) Li–CNT40 after stripping, as indicated in the scheme of the voltage profiles in the middle of the figure. Cross-sectional images obtained via cryo-FIB-SEM are depicted for lithium and Li–CNT40 in e,f) pristine state as well as g,h) after stripping, respectively.

It was shown in Figure 3 that stripping is quite similar for lithium and Li–CNT up to the point, where pure lithium shows severe polarization due to formed pores at the interface, that is, due to current constriction at the remaining contact spots. The kink in the voltage profile for Li–CNT electrodes, which indicates that the stripping mechanism changes, occurs at quite the same time. This suggests that lithium from the composite is at first dissolved during stripping at the direct interface to the SE. At the time where the kink appears, this direct interface is depleted. From that point on, the CNTs act as a contact mediator, maintaining contact to the SE and acting as a 3D distributed anode scaffold. Another effect at play could be the increased ionic conductivity of contact spots due to Joule heating,[44] which may be one explanation for the improved stripping after the kink.

The difference in pore geometry also influences the low-frequency impedance shown in Figure 2b. As the pore geometry is different, the contribution of surface diffusion of lithium atoms, which typically occurs in that frequency range, is different for lithium and the composites. This results in the more flattened semicircle for Li–CNT30. Note that stripping experiments were additionally carried out with Li-vapor grown carbon fibers (VGCF) composite electrodes. With VGCF, Figure S7, Supporting Information, shows no improvement compared to lithium. We believe that this highlights the favorable role of transport along the graphitic walls of the CNTs.

Due to the continued stripping both through and at the walls of the CNTs, lithium is dissolved also inside the bulk of the electrode and not only at the interface, leading to closed porosity as seen in Figure 4. The proposed stripping mechanism is schematically depicted in **Figure 5**.

While the observed change to 3D stripping for the composite electrodes leads to a higher anode utilization, mixing lithium with additives inevitably leads to a decrease in the anode's theoretical specific capacity. As these effects counteract each other, there exists an optimum in the composition of the composite electrode, which is around 30 wt% of CNTs according to the stripping profiles provided in Figure 3a. The theoretical specific capacity of Li–CNT30 then amounts to around 2819 mAh g^{-1} of which 60% could be stripped with 100 µA cm^{-2}. This value well surpasses alternative electrode concepts, such as porous garnet SE infiltrated with lithium metal.[20]

2.4. Mechanics of Composite Anodes and Influence on Electrode Kinetics

Incorporating fibers into a ductile matrix can lead to very strong changes in the mechanical properties.[52,53] For example, Fu et al. specify that for fibers to have an impact on the strength when randomly distributed in a matrix, a critical fiber length

$$l_c = \frac{\sigma_f \cdot d}{2\tau_m} \tag{1}$$

must be exceeded.[52,54] Herein, σ_f and d denote the fiber tensile strength and diameter, respectively, whereas τ_m denotes the shear yield strength of the matrix, if lower than the bonding strength between the phases. With around 5 µm, the herein used CNTs in lithium exceed the calculated l_c of 128 nm by a factor of 40. This suggests that CNTs have a large impact on the composite anode elastic and plastic properties, as already assumed from the changes in ductility noticed during sample preparation.

In another example, the elastic modulus of matrices is strongly increased by the reinforcing integration of constituents with relatively high elastic modulus, for example, by adding carbon fibers to an epoxy matrix to form carbon-reinforced composites.[55] The orientation and volume fraction of the reinforcing (higher elastic modulus) constituent is important in determining whether or not a composite has isotropic or anisotropic mechanical properties. The goal of the present study was to homogeneously disperse CNTs, thus effectively resulting in isotropic properties. However, it is possible that the homogeneity of CNT distribution decreases above a certain volume fraction of CNTs as was suggested by the unexpected deviation in electrochemical performance when increasing from 30–40 wt% CNT.

To investigate the plastic and elastic properties of the composites, compressive and tensile stress–strain testing was carried out on prepared pellets and foils, respectively. These measurements were conducted with a strain rate of 10^{-3} mm s^{-1} in accordance with Masias et al.[56,57] Results are depicted in **Figure 6**a,b.

The stress–strain curves obtained during compression show a decrease in yield strength of flow stress with increasing

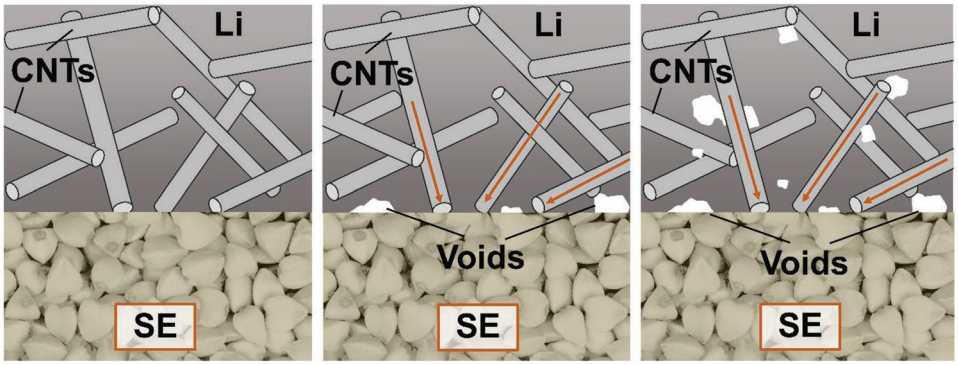

Figure 5. Schematic depiction of the lithium stripping process of composite anodes consisting of lithium and CNTs. During stripping, the direct interface between lithium and LLZO is first depleted as in the case of pure lithium electrodes (middle). However, instead of fully losing the contact like pure lithium, the composites allow also stripping along the remaining CNTs, which act as a contact mediator (right). Note that the pores and CNTs are not scaled 1:1 with respect to their true size.

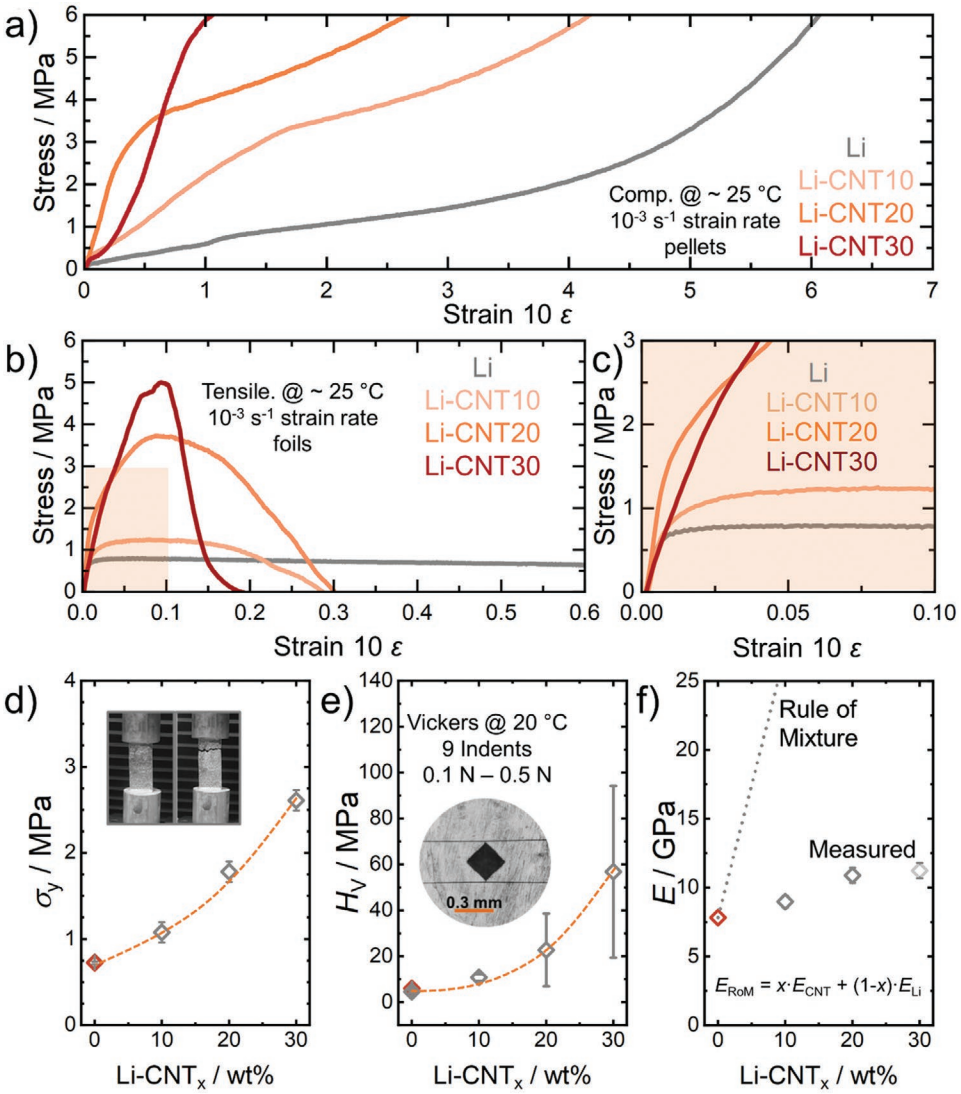

Figure 6. a) Compressive stress–strain results for composite pellets. b) Tensile stress–strain tests for composite foils (150 µm) with the orange inset enlarged in (c). Results are also shown for d) the yield strength σ_y, e) the Vickers hardness H_V, and f) the elastic modulus E. The inset in (d) shows an example of the mechanical tensile tests and the inset in (e) shows an indentation mark typically observed after testing of H_V. Literature values are presented as orange data points.

CNT content. In general, the stress required to increase strain increases with increasing strain. However, the data in Figure 6a are engineering strain and do not consider the increase in sample area. It appears that the characteristic yield inflection point in Figure 6a is found at higher stresses for higher amounts of CNTs. However, the initial shift in strain of the measurement for Li–CNT30, compared to the Li–CNT10 and Li–CNT20, seems to be out of the expected trend. This likely is the result of inhomogeneity within the composites at higher CNT fractions. In addition, after the initial shift in strain, the Li–CNT30 composite has approximately the same stress–strain slope as the Li–CNT20, thus indicating that point of diminishing return for the stiffness is achieved between 20 wt% and 30 wt% CNT. We refrain from including mechanical testing data on Li–CNT40, as large specimens of Li–CNT40 needed for stress-strain measurements, are too heterogeneous to afford conclusive results for mechanical testing, even though it was possible to obtain reproducible electrochemical performance with such a large fraction of CNTs.

During tensile testing, a trend is observed with increasing CNT content that is similar to that of compression testing. The most obvious differences between the composites and pure lithium are strength maxima, which get increasingly more pronounced with higher CNT contents (up to 5 MPa for Li–CNT30). Likely, these are caused by an effect similar to molecular chain alignment in polymers during tensile testing or fiber alignment in carbon-fiber reinforced composites,[58] which arises due to originally randomly oriented CNTs in the metal matrix lining up with deformation. Such an alignment usually strengthens fiber-in-matrix composites.[52,59] However, according to Masias et al., elastic properties cannot be extracted from stress–strain measurements of lithium metal,

as plastic deformation overlaps with the elastic regime, which results in a large underestimation of the elastic modulus.[56] Creep likely affects the results as well, which is indicated by the high homologous temperature of 0.66 of lithium at room temperature.

Additionally, Figure 6c depicts the low strain-regime during tensile testing, which shows that the first inflection point in these graphs occurs at a later stage for higher CNT contents. These inflection points are interpreted as the yield strength or flow stress.[56,59] The estimated yield strength σ_y is summarized in Figure 6d and increases with higher CNT content. Note that the yield strength for pure lithium fits to literature values,[56] which are included as orange data points. Also shown are the Vickers hardness, H_V, in Figure 6e and estimated elastic moduli, E, in Figure 6f. The latter was obtained from acoustic measurements; please see Figure S8, Supporting Information, for more information.

Like the general stiffness of the material, both the yield strength σ_y and Vickers hardness H_V increase with CNT content. Note that the Vickers hardness measurement error obtained from the standard deviation is significantly higher for Li–CNT20 and Li–CNT30. This signals inhomogeneity within the samples with higher CNT content as already assumed above. In samples with 30 wt% CNT, σ_y and H_V increased to 2.61 and 56.8 MPa, respectively, which fits to the previously made observation that the material is mechanically strengthened by the incorporation of CNTs.

The elastic modulus E displayed in Figure 6f obtained from acoustic measurements shows a similar trend to H_V and σ_y. Interestingly, E does not follow the values that would be obtained from a simple rule of mixture. This underlines the assumption that the CNTs are not perfectly and homogeneously dispersed within the lithium matrix and accumulate locally, as already seen in the hardness tests. The increase in E deviates from linearity for the step between 20 and 30 wt%, yielding a lower value than expected, which strengthens this assumption. Still, an increase of E up to 11.2 GPa is observed for Li–CNT30. Note that usually single-phase or homogeneous materials are characterized using indentation and acoustic analysis of the elastic properties. However, the large area of the indent (200 µm × 200 µm) and the acoustic wavelength of around 6 m in lithium at 1 kHz averages the observed properties,[60] as the tubes are only 5 µm in length.

Our results show that the mechanical properties of lithium metal can be well tailored by the addition of small quantities of CNTs. In this way, anodes can be engineered to be less sensitive to external stack pressures. To showcase this concept, a lithium and a Li–CNT30 anode were stripped for 4 h without any applied pressure. Afterward, a stack pressure of 3.0 MPa was applied and then gradually decreased until 0.5 MPa as depicted in **Figure 7**a. This method yields the critical stack pressure needed for an electrode material to counteract the strain induced by stripping with a certain current density.[15]

At the end of the pressure-free stripping step after 4 h, the lithium electrode shows a higher polarization. When 3.0 MPa are applied thereafter, a large decrease in polarization occurs for lithium while polarization of Li–CNT30 remains nearly constant. This is explained by the pressure-induced closing of the pores at the Li|LLZO interface, which have not yet formed at the

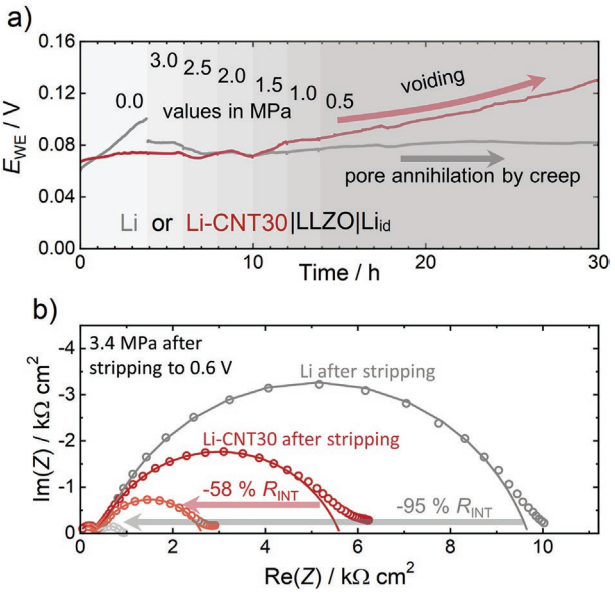

Figure 7. a) Voltage profiles of a lithium and a Li–CNT30 electrode during stripping with 100 µA cm^{-2} in combination with a gradual decrease in applied stack pressure. b) Impedance spectra of both Li|LLZO|Li and Li|LLZO|Li–CNT30 directly after pressure-free stripping to 0.6 V and applying 3.4 MPa.

Li–CNT30|LLZO interface. This highlights Li–CNT30 being less dependent on and sensitive to applied stack pressures.

However, while 0.5 MPa pressure applied in the last stage during stripping seems to be enough to counteract strain-induced at 100 µA cm^{-2} for pure lithium, an increase in voltage for the composite begins. This means that pores form, which are not annihilated by creep due to the higher resistance to plastic deformation of the composite.

The higher pressure-sensitivity of pure lithium can also be seen in the Nyquist plots depicted in Figure 7b. Here, the impedance spectra of both lithium and Li–CNT directly after stripping until 0.6 V and after applying 3.4 MPa are plotted. The decrease in R_{INT} is far larger for lithium (91%) than for Li–CNT30 (58 %). The reason is that pure lithium is more easily deformed, allowing it to regain good contact to the SE. However, the pore geometry is different when considering Li–CNT composites as shown via cross-sectional imaging above. This may require higher pressures to collapse pores independent of the ductility of the material.

3. Conclusions

We showcase the tunability of electrochemical and mechanical properties of the lithium metal anode by manufacturing a composite material with CNTs. It is found that the areal discharge (stripping) capacity can be enhanced by a factor of >20 to around 25 mAh cm^{-2} at 100 µA cm^{-2} and low pressures (<1 MPa) by extending the lithium dissolution from the direct electrode|LLZO (2D) interface to the 3D Li–CNT network, albeit at higher electrode potentials E_{WE} > 0.5 V. This amounts to about 60% of the theoretical specific capacity of 2819 mAh g^{-1} calculated for Li–CNT30. Cross-sectional

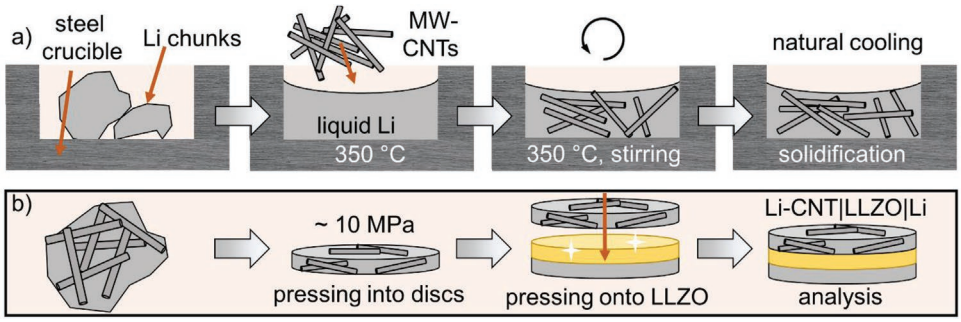

Figure 8. Scheme of a) the preparation route to obtain Li–CNT composites and b) electrode preparation and attachment to a polished LLZO pellet for electrochemical analysis.

micrographs obtained with cryo-FIB-SEM prove stripping within the bulk of the anode, guided by CNTs in the composite. The CNT framework clearly helps to maintain electrical contact with LLZO during stripping. Additionally, a twofold increase of the effective diffusion coefficient in the anode material to around $D_{\text{eff}} = (1.3 \pm 0.3) \times 10^{-11}$ cm^2 s^{-1} for Li–CNT30 was estimated from stripping and depletion experiments. Stress–strain measurements show a decrease in the ductility of the composite based on its CNT content, which is confirmed by microindentation and acoustic analysis. For example, the Vickers hardness and the elastic modulus increase to nearly 60 MPa and 12 GPa, which represents an eightfold and 60% increase relative to pure lithium, respectively.

This tunability of the electrochemo-mechanical properties of the LMA presents an attractive route of tailoring the anode material to suit the requirements of practical applications. For example, Li–CNT electrodes would be suitable for high-energy applications without the possibility of applying stack pressures. As a large fraction of the available discharge capacity is only available with an overvoltage >0.5 V, pure lithium is more suitable for high-power applications, especially when stack pressure can be applied due to its more ductile nature.

4. Experimental Section

Preparation of Solid Electrolytes and Composite Electrodes: The nominal composition of the herein prepared LLZO:Al, based on the used precursors, was $Li_{6.25}Al_{0.25}La_3Zr_2O_{12}$ (LLZO). First, Li_2CO_3 (>99.0 %, Sigma-Aldrich), ZrO_2 (99.9%, Sigma-Aldrich), $La(OH)_3$ (99.9 %, Sigma-Aldrich), and Al_2O_3 (99.8 %, abcr) were homogenized with two ball-milling steps (10 min with 20 min pause at 350 rpm, 24 cycles). Subsequent calcination of 25 mm diameter pellets was carried out in MgO-crucibles under oxygen flow (150 sccm) by heating the material up to 1000 °C, which was held for 4 h. The following steps were exclusively performed under an argon environment (MBraun, <0.1 ppm H_2O, <0.1 ppm O_2). First, to obtain small particles for sintering, the material was ball-milled with the same parameters as above for 40 cycles. Pellets were then sintered (isostatically pressed beforehand, 380 MPa) under oxygen flow in MgO-crucibles with mother powder (calcined LLZO powder). For this, samples were first heated in 9 h to 900 °C, which was held for 5 h. Thereafter, the temperature was increased in 2 h to 1100 °C and again held for 5 h. Last, in 1 h, the temperature was increased again to 1230 °C and held for 4 h, followed by a natural cooling. For CCD tests, LLZO:Ta ($Li_{6.5}La_3Ta_{0.5}Zr_{1.5}O_{12}$) was used, which was prepared as previously reported by Taylor et al.[61]

Composite electrodes were prepared by homogeneously dispersing CNTs (Sigma Aldrich, >95%, 6–9 nm × 5 µm) into liquid lithium at 350 °C on a hotplate inside a glovebox. After solidification of the mixture, small chunks of the material were cut off with a ceramic knife and pressed into disc electrodes with 6 mm in diameter and around 120 µm thickness. Prepared electrodes were described, for example, with "Li–CNT30," meaning that 30 wt% of CNTs was nominally mixed into liquid lithium. This procedure is schematically depicted in **Figure 8**.

Material Characterization: Structural characterization of LLZO was performed using a PANalytical Empyrean powder diffractometer in Bragg–Brentano θ–θ geometry with Cu K_α radiation (λ_1 = 1.5405980 Å; λ_2 = 1.5444260 Å; $I(\lambda_2)/I(\lambda_1) = 0.5$). Measurements were carried out in the 2θ range between 20° and 80° with a step size of 0.026°. Air-sensitive samples were protected with thin Kapton foil during the measurement.

Cell Assembly and Electrochemical Characterization: Cells were assembled by polishing the garnet pellets with grit P1000 SiC-paper and subsequent electrode attachment. Both pure lithium and composite electrodes were freshly pressed into thin foils. As a counter electrode, a resistance-free, ideally reversible electrode Li_{id} was prepared following previous reports utilizing high isostatic pressure (380 MPa for 30 min).[8,37] Composite electrodes were attached to the SE by a small hand-pressing tool under an applied torque of 10 N m. Cells used for testing the CCD were prepared by polishing the Ta:LLZO following the procedures of Sharafi et al.,[39] and then heat treating and applying lithium electrodes following the procedures of Wang et al.[15]

Electrochemical characterization was carried out using a VMP300 potentiostat by BioLogic in combination with the software EC-Lab (V. 11). Temperature dependent measurements were carried out in a climate chamber WKL 64 by WEISS. For electrochemical measurements, cells were contacted with nickel current collector tabs and sealed in pouch cells. The current collector tabs were fixed using small clamps to secure contact to the electrodes. Please note, however, that by the use of this setup, the clamps exerted a small pressure (<1 MPa) to maintain the current collectors in place, which was much lower than reported before and was therefore addressed here as pressure-free.

If not stated otherwise, potentiostatic electrochemical impedance spectroscopy (PEIS) measurements were carried out in the frequency range between 7 MHz and 100 mHz. GEIS measurements were carried out in a different frequency range, 7 MHz–1 Hz, as acquisition of one spectrum needed to be faster in this measurement mode to not disturb the DC current. Usually, 10% of the DC current was used as amplitude to measure the impedance response of the cell. Impedance data interpretation as well as fitting thereof was carried out with RelaxIS 3 software by RhD Instruments.

FIB-SEM Measurements: FIB-SEM imaging was carried out using a XEIA3 GMU SEM/Plasma-FIB (Tescan) in combination with a Leica VCT500 transfer module and liquid nitrogen cooling stage. SEM imaging was also carried out using a Zeiss Merlin HRSEM.

Mechanical Property Characterization: Mechanical property testing was carried out in an argon-filled glovebox using an Instron 5944 Universal Testing System. The compression tests were carried out according to Masias et al. with a strain rate of 10^{-3} s^{-1}.[56] To mitigate friction between the sample and the testing device, mineral oil was used as coupling agent. Tensile tests were also carried out using the strain rate of 10^{-3} s^{-1}.

Samples were fixed onto the testing device using acrylate-based adhesive. Note that for all graphs the engineering strain was used, which was calculated based on the initial cross-sectional area of the sample.

Both testing of the Vickers hardness and acoustic measurements were performed in a dry room on lithium foil ($T_d < -50$ °C). The micro-indentation tests were carried out with a Vickers hardness tester (HM122V/K Series 810 Micro, Mitutoyo Corporation) using 0.01–0.05 kgf to indent 200 µm thick anode foils, which were previously rolled using a calendaring machine (Creative and Innovative System Corporation). Pulse echo acoustic measurements were carried out using Olympus 5073R Pulser/Receiver (P/R) paired with a Picoscope 2207A PC-based oscilloscope. Longitudinal wave speeds were measured using an Olympus M110-RM contact transducer with mineral oil as a coupling agent to the sample.

Supporting Information

Supporting Information is available from the Wiley Online Library or from the author.

Acknowledgements

The authors want to thank Dr. Boris Mogwitz for help with FIB-SEM measurements. This work was conducted as part of the US–German joint collaboration on "Interfaces and Interphases in Rechargeable Li-metal-based Batteries" supported by the US Department of Energy (DOE) and German Federal Ministry of Education and Research (BMBF). This work has been partly funded by the German Federal Ministry of Education and Research (BMBF) under the project "LiSI," grant identifier 03XP0224E. Financial support from the DOE under the project "CatSE," grant number DE-ACO5-000R22275, is acknowledged.

Open access funding enabled and organized by Projekt DEAL.

Conflict of Interest

The authors declare no conflict of interest.

Data Availability Statement

The data that support the findings of this study are available from the corresponding author upon reasonable request.

Keywords

carbon nanotubes, composite lithium-anodes, diffusion, mechanical properties, three-dimensional lithium dissolution

Received: April 1, 2022
Revised: April 25, 2022
Published online: May 31, 2022

[1] J. Janek, W. G. Zeier, *Nat. Energy* **2016**, *1*, 16141.
[2] S. Randau, D. A. Weber, O. Kötz, R. Koerver, P. Braun, A. Weber, E. Ivers-Tiffée, T. Adermann, J. Kulisch, W. G. Zeier, F. H. Richter, J. Janek, *Nat. Energy* **2020**, *5*, 259.
[3] Y. Lee, S. Fujiki, C. Jung, N. Suzuki, N. Yashiro, R. Omoda, D. Ko, T. Shiratsuchi, T. Sugimoto, S. Ryu, J. H. Ku, T. Watanabe, Y. Park, Y. Aihara, D. Im, I. T. Han, *Nat. Energy* **2020**, *5*, 299.
[4] T. Krauskopf, F. H. Richter, W. G. Zeier, J. Janek, *Chem. Rev.* **2020**, *120*, 7745.
[5] Y. Zhu, X. He, Y. Mo, *ACS Appl. Mater. Interfaces* **2015**, *7*, 23685.
[6] Y. Chen, Z. Wang, X. Li, X. Yao, C. Wang, Y. Li, W. Xue, D. Yu, S. Y. Kim, F. Yang, A. Kushima, G. Zhang, H. Huang, N. Wu, Y. W. Mai, J. B. Goodenough, J. Li, *Nature* **2020**, *578*, 251.
[7] C. Niu, H. Lee, S. Chen, Q. Li, J. Du, W. Xu, J. G. Zhang, M. S. Whittingham, J. Xiao, J. Liu, *Nat. Energy* **2019**, *4*, 551.
[8] T. Krauskopf, H. Hartmann, W. G. Zeier, J. Janek, *ACS Appl. Mater. Interfaces* **2019**, *11*, 14463.
[9] T. Krauskopf, B. Mogwitz, H. Hartmann, D. K. Singh, W. G. Zeier, J. Janek, *Adv. Energy Mater.* **2020**, *10*, 2000945.
[10] E. Kazyak, S. William, C. Haslam, J. Sakamoto, N. P. Dasgupta, E. Kazyak, R. Garcia-mendez, W. S. Lepage, A. Sharafi, A. L. Davis, A. J. Sanchez, K. Chen, C. Haslam, J. Sakamoto, N. P. Dasgupta, *Matter* **2020**, *2*, 1025.
[11] I. Seymour, A. Aguadero, *J. Mater. Chem. A* **2021**, *9*, 19901.
[12] S. S. Shishvan, N. A. Fleck, V. S. Deshpande, *J. Power Sources* **2021**, *488*, 229437.
[13] U. Roy, N. A. Fleck, V. S. Deshpande, *Extreme Mech. Lett.* **2021**, *46*, 101307.
[14] J. Janek, S. Majoni, *Ber. Bunsen-Ges. Phys. Chem.* **1995**, *99*, 14.
[15] M. J. Wang, R. Choudhury, J. Sakamoto, *Joule* **2019**, *3*, 2165.
[16] X. Zhang, Q. J. Wang, K. L. Harrison, S. A. Roberts, S. J. Harris, *Cell Rep. Phys. Sci.* **2019**, *1*, 100012.
[17] T. Krauskopf, B. Mogwitz, C. Rosenbach, W. G. Zeier, J. Janek, *Adv. Energy Mater.* **2019**, *9*, 1902568.
[18] G. T. Hitz, D. W. McOwen, L. Zhang, Z. Ma, Z. Fu, Y. Wen, Y. Gong, J. Dai, T. R. Hamann, L. Hu, E. D. Wachsman, *Mater. Today* **2019**, *22*, 50.
[19] S. Xu, D. W. McOwen, C. Wang, L. Zhang, W. Luo, C. Chen, Y. Li, Y. Gong, J. Dai, Y. Kuang, C. Yang, T. R. Hamann, E. D. Wachsman, L. Hu, *Nano Lett.* **2018**, *18*, 3926.
[20] C. Wang, Y. Gong, B. Liu, K. Fu, Y. Yao, E. Hitz, Y. Li, J. Dai, S. Xu, W. Luo, E. D. Wachsman, L. Hu, *Nano Lett.* **2017**, *17*, 565.
[21] K. K. Fu, Y. Gong, B. Liu, Y. Zhu, S. Xu, Y. Yao, W. Luo, C. Wang, S. D. Lacey, J. Dai, Y. Chen, Y. Mo, E. Wachsman, L. Hu, *Sci. Adv.* **2017**, *3*, e1601659.
[22] H. Xie, C. Yang, Y. Ren, S. Xu, T. R. Hamann, D. W. Mcowen, E. D. Wachsman, L. Hu, *Nano Lett.* **2021**, *21*, 6163.
[23] A. Sharafi, E. Kazyak, A. L. Davis, S. Yu, T. Thompson, D. J. Siegel, N. P. Dasgupta, J. Sakamoto, *Chem. Mater.* **2017**, *29*, 7961.
[24] N. Nitta, G. Yushin, *Part. Part. Syst. Charact.* **2014**, *31*, 317.
[25] D. Lin, Y. Liu, Z. Liang, H. W. Lee, J. Sun, H. Wang, K. Yan, J. Xie, Y. Cui, *Nat. Nanotechnol.* **2016**, *11*, 626.
[26] J. Zhao, G. Zhou, K. Yan, J. Xie, Y. Li, L. Liao, Y. Jin, K. Liu, P. C. Hsu, J. Wang, H. M. Cheng, Y. Cui, *Nat. Nanotechnol.* **2017**, *12*, 993.
[27] H. Chen, Y. Yang, D. T. Boyle, Y. K. Jeong, R. Xu, L. S. de Vasconcelos, Z. Huang, H. Wang, H. Wang, W. Huang, H. Li, J. Wang, H. Gu, R. Matsumoto, K. Motohashi, Y. Nakayama, K. Zhao, Y. Cui, *Nat. Energy* **2021**, *6*, 790.
[28] A. S. Cavanagh, C. A. Wilson, A. W. Weimer, S. M. George, *Nanotechnology* **2009**, *20*, 255602.
[29] Y. Maniwa, R. Fujiwara, H. Kira, H. Tou, E. Nishibori, M. Takata, M. Sakata, A. Fujiwara, X. Zhao, S. Iijima, S. Iijima, Y. Ando, *Phys. Rev. B: Condens. Matter Mater. Phys.* **2001**, *64*, 731051.
[30] A. N. Popova, *Coke Chem.* **2017**, *60*, 361.
[31] B. E. Warren, *Phys. Rev.* **1941**, *59*, 693.
[32] S. Schweidler, L. De Biasi, A. Schiele, P. Hartmann, T. Brezesinski, J. Janek, *J. Phys. Chem. C* **2018**, *122*, 8829.
[33] V. Petkov, A. Timmons, J. Camardese, Y. Ren, *J. Phys.: Condens. Matter* **2011**, *23*, 435003.
[34] Y. Shao, H. Wang, Z. Gong, D. Wang, B. Zheng, J. Zhu, Y. Lu, Y. S. Hu, X. Guo, H. Li, X. Huang, Y. Yang, C. W. Nan, L. Chen, *ACS Energy Lett.* **2018**, *3*, 1212.
[35] J. Duan, Y. Zheng, W. Luo, W. Wu, T. Wang, Y. Xie, S. Li, J. Li, Y. Huang, *Natl. Sci. Rev.* **2020**, *7*, 1208.

[36] D. N. Futaba, T. Yamada, K. Kobashi, M. Yumura, K. Hata, *J. Am. Chem. Soc.* **2011**, *133*, 5716.
[37] T. Fuchs, B. Mogwitz, S. Otto, S. Passerini, F. H. Richter, J. Janek, *Batteries Supercaps* **2021**, *4*, 1145.
[38] J. T. S. Irvine, D. C. Sinclair, A. R. West, *Adv. Mater.* **1990**, *2*, 132.
[39] A. Sharafi, C. G. Haslam, R. D. Kerns, J. Wolfenstine, J. Sakamoto, *J. Mater. Chem. A* **2017**, *5*, 21491.
[40] Y. Matsuki, K. Noi, M. Deguchi, A. Sakuda, A. Hayashi, M. Tatsumisago, *J. Electrochem. Soc.* **2019**, *166*, A5470.
[41] P. Albertus, S. Babinec, S. Litzelman, A. Newman, *Nat. Energy* **2018**, *3*, 16.
[42] H. J. S. Sand, *London, Edinburgh Dublin Philos. Mag. J. Sci.* **1901**, *1*, 45.
[43] L. Stolz, G. Homann, M. Winter, J. Kasnatscheew, *Mater. Today* **2021**, *44*, 9.
[44] R. D. Rogler, H. Löbl, J. Schmidt, *Eur. Trans. Electr. Power* **1997**, *7*, 331.
[45] K. D. Kim, D. D. L. Chung, *J. Electron. Mater.* **2002**, *31*, 933.
[46] T. H. Loeber, B. Laegel, S. Wolff, S. Schuff, F. Balle, T. Beck, D. Eifler, J. H. Fitschen, G. Steidl, *J. Vac. Sci. Technol., B: Nanotechnol. Microelectron.: Mater., Process., Meas., Phenom.* **2017**, *35*, 06GK01.
[47] F. Santoro, E. Neumann, G. Panaitov, A. Offenhäusser, *Microelectron. Eng.* **2014**, *124*, 17.
[48] S. Liu, L. Sun, J. Gao, K. Li, *J. Microsc.* **2018**, *272*, 3.
[49] D. P. Adams, T. M. Mayer, M. J. Vasile, K. Archuleta, *Appl. Surf. Sci.* **2006**, *252*, 2432.
[50] G. Ran, J. Zhang, Q. Wei, S. Xi, X. Zu, L. Wang, *Appl. Phys. Lett.* **2009**, *94*, 2007.
[51] I. Koponen, M. Hautala, O. P. Sievänen, *Phys. Rev. Lett.* **1997**, *78*, 2612.
[52] W. D. Callister, *Materials Science and Engineering: An Introduction*, 8th ed., Wiley, Hoboken, NJ, USA **2009**.
[53] P. Barai, G. J. Weng, *Int. J. Plast.* **2011**, *27*, 539.
[54] S.-Y. Fu, B. Lauke, *Compos. Sci. Technol.* **1996**, *56*, 1179.
[55] I. J. Beyerlein, S. L. Phoenix, *Compos. Sci. Technol.* **1996**, *56*, 75.
[56] A. Masias, N. Felten, R. Garcia-Mendez, J. Wolfenstine, J. Sakamoto, *J. Mater. Sci.* **2018**, *54*, 2585.
[57] A. Masias, N. Felten, J. Sakamoto, *J. Mater. Res.* **2021**, *36*, 729.
[58] W. S. LePage, Y. Chen, E. Kazyak, K.-H. Chen, A. J. Sanchez, A. Poli, E. M. Arruda, M. D. Thouless, N. P. Dasgupta, *J. Electrochem. Soc.* **2019**, *166*, A89.
[59] P. K. Mallick, *Fiber-Reinforced Composites*, Taylor & Francis Group, LLC, Boca Raton, FL, USA **2007**.
[60] E. G. Herbert, S. A. Hackney, V. Thole, N. J. Dudney, P. S. Phani, *J. Mater. Res.* **2018**, *33*, 1347.
[61] N. J. Taylor, S. Stangeland-Molo, C. G. Haslam, A. Sharafi, T. Thompson, M. Wang, R. Garcia-Mendez, J. Sakamoto, *J. Power Sources* **2018**, *396*, 314.